Chemical Science

ROYAL SOCIETY OF CHEMISTRY

EDGE ARTICLE

View Article Online
View Journal | View Issue

Cite this: *Chem. Sci.*, 2024, **15**, 9630

All publication charges for this article have been paid for by the Royal Society of Chemistry

Engineered solid-state aggregates in brickwork stacks of n-type organic semiconductors: a way to achieve high electron mobility†

Indrajit Giri,[a] Shant Chhetri,[a] Jesslyn John P.,[a] Madalasa Mondal,[a] Arka Bikash Dey[b] and Ratheesh K. Vijayaraghavan *[a]

Received 9th April 2024
Accepted 16th May 2024

DOI: 10.1039/d4sc02339k

rsc.li/chemical-science

Efficient, economically viable n-type organic semiconductor materials suitable for solution-processed OFET devices with high electron mobility and ambient stability are scarce. Merging these attributes into a single molecule remains a significant challenge and a careful molecular design is needed. To address this, synthetic viability (achievable in fewer than three steps) and using cost-effective starting materials are crucial. Our research presents a strategy that meets these criteria using naphthalene diimide (NDI) core structures. The approach involves a simple synthesis process with a cost of $ 5–10 per gram for the final products. This paper highlights our success in scaling up the production using affordable known reagents, creating ambient condition solution-processed OFET devices with impressive electron mobility, on–off current ratio (1 $cm^2\ V^{-1}\ s^{-1}$ and $I_{on}/I_{off} \sim 10^9$) and good ambient stability (more than 100 h). We conducted a comprehensive study on $EHNDIBr_2$, a material that demonstrates superior performance due to its unique supramolecular arrangement in its brickwork stack. This was compared with two similar structures to validate our findings. The superior performance of $EHNDIBr_2$ is attributed to the effective interlocking of charge-hopping units within the NDI core in its brickwork stack. Our findings include detailed electronic, spectroscopic, and microscopic analyses of these layers.

Introduction

In the past decade, significant progress has been made in developing n-type molecular semiconductors with efficient charge transport properties.[1] Due to the possibility of diversifying molecular features and obtaining the desired functional outcome suitable for various electronic devices, immense efforts have been made towards developing new materials.[2–6] Apart from focusing on molecular features, their solid-state packing and supramolecular structures are equally significant in deciding their charge transport properties.[7–10] In the supramolecular arrangement, the relative position and magnitude of molecular displacement immensely influence (i) the intermolecular frontier molecular orbital overlap, (ii) the electronic structure and state energies, and (iii), thereby, the bulk charge carrier transport. Such interconnected complex parameters in the supramolecular structure necessitate tedious effort to unravel their roles in charge transport. From the point of view of molecular packing, widely recognized promising molecular packing motifs for efficient carrier transport include herringbone and a brickwork structure.[10,11]

Molecular aggregates formed by weak intermolecular interactions would yield mechanically flexible active layers and devices.[12,13a,b] The intrinsic solubility and processibility of such materials are also eventually determined by such non-covalent interactions. In many cases, such strong and cooperative interactions adversely affect the processibility. Hence, it is highly recommended to have a balance to achieve such conflicting requirements, and it is essential to address these non-covalent interactions at the molecular level and tailor them to obtain the desired materials with suitable carrier transport.[13c] Additionally, in systems with poorly managed molecular ordering due to the lack of appropriate functional groups to benefit such non-covalent interactions, thermally induced lattice vibrations and, thereby, lowering of charge carrier transport are well known. Hence, reduction of dynamic disorder by engineered supramolecular lattice assembly and crystalline active layers are essential to achieve high performance in semiconductor devices. There are some recent reports in the abovementioned directions.[14–18] Some molecular semiconductors and OFETs derived from them have exhibited benchmark performance in laboratory scale devices. Most of them fall into p-type materials.[19–22] N-type materials developed by an easy synthetic strategy and less expensive chemicals are

[a]*Department of Chemical Sciences, Indian Institute of Science Education and Research, Mohanpur, Kolkata, 741246, India. E-mail: ratheesh@iiserkol.ac.in*

[b]*Deutsches Elektronen-Synchrotron DESY, Notkestr. 85, 22607, Hamburg, Germany*

† Electronic supplementary information (ESI) available: Synthesis, crystallography, and characterization. CCDC 2323962, 2323963 and 2346855. For ESI and crystallographic data in CIF or other electronic format see DOI: https://doi.org/10.1039/d4sc02339k

essential for the mass production and wide use of such materials. Hence, our comprehensive approach to tackle most of these requirements is summarized here. Complex electron-deficient backbones are purposefully excluded from the molecular design due to the complex synthetic routes that limit the scalability. Special attention was devoted to designing the molecular structure to yield multiple intermolecular solid-state interactions to minimize the longitudinal slip, thereby reducing the free volume in the crystal lattice and, hence, the lattice vibrations. Synthetic easiness was also given equal importance to ensure the scalability and economic utility of these materials. The desired functional group should also favour operational and ambient stability and effective solid-state aggregation crucial in achieving high carrier mobility. Substitution of planar aromatics with electron-withdrawing functional groups or electronegative atoms to yield n-type molecular semiconductor materials is a known concept.[23–26] However, apart from orbital engineering, a comprehensive approach to understand the role of functional groups in dictating solid-state molecular packing and, thereby, efficient charge hoping still warrants careful attention. Some random design concepts and examples are known along similar lines of thought, but a lucid approach to investigate the structural features is limited. Primarily, such atoms or groups should endorse a deep LUMO to ensure efficient electron injection at a low operational bias and favour substantial non-covalent interactions in their aggregated superstructures. Despite fluorine (F) being the most electronegative atom, chlorine (Cl) and bromine (Br) are also efficient in lowering the LUMO due to the presence of the empty d orbitals, making them better π-acceptors.[27] They are more efficient in enhancing non-covalent interactions due to better polarizability and large van-der Waals radii, enhancing the in-plane structural rigidity.[28] The significance of such planar interactions and the resultant rigid frameworks in reducing the lattice vibrations and electron scattering would be essential for better carrier transport and electron mobility.[14] This report addresses the importance of such 3-D structural motifs in self-assembled structures of molecular semiconductors.

Results and discussion

Structural features and synthesis

For our core units, we prioritize features like a low-lying LUMO, distinct optical signatures to track the self-assembly, reversible redox properties, ambient stability, and well-organized aggregated structures, making naphthalene diimides (NDIs) an ideal choice. NDIs offer ease of functionalization and the addition of end groups. Incorporating bromine (Br) atoms into the backbone (EHNDI → $EHNDIBr_2$ → $EHNDIBr_4$) is expected to lower the LUMO and create diverse in-plane C–H···Br hydrogen bond interactions. Notably, $EHNDIBr_4$ forms brickwork stacks without lateral C–H···Br interactions due to the absence of a corresponding hydrogen bond donor. These molecules were synthesized through known synthetic routes in two to three steps (Scheme 1a),[29] yielding 25–80% (EHNDI–$EHNDIBr_4$). The cost per gram of $EHNDIBr_2$ is approximately 6–8 USD. The synthesis involved reacting commercially available naphthalenetetracarboxylic dianhydride (NDA) with 1,3-dibromo-5,5-dimethylhydantoin (DBH) in concentrated H_2SO_4, followed by a reaction in acetic acid with (±)2-ethyl-1-hexylamine (EHA) to obtain the imide compounds (racemic mixture of the amine was used). This might yield the following combinations of products (R–R, S–S, R–S/S–R). The tetra-bromo derivative required an additional step of refluxing with PBr_3 in toluene. All compounds were further purified by column chromatography. Detailed synthetic procedures and characterization data are available in the ESI (Scheme S1†). The resulting solids were white (EHNDI), pale yellow ($EHNDIBr_2$), and orange ($EHNDIBr_4$), with purity confirmed by TLC, ^{1}H NMR, and single crystal X-ray analysis. Single crystals of $EHNDIBr_2$ and $EHNDIBr_4$ were grown using solvent evaporation methods from specific solvent mixtures of chloroform and *ortho*-dichloro benzene (*o*-DCB) (9 : 1). After several attempts, EHNDI single crystals were successfully grown for diffraction, albeit with poor crystal quality, through the slow solvent (ethanol) diffusion process into a solution of chloroform and ethanol mixture (2 : 1). Interestingly, single crystals of all derivatives yielded the 'meso' product (R, S/S, R). Here, the focus is not on the chirality of the sidechains or its intriguing effects on crystallinity, morphology and electron transport. A detailed study in those aspects is in progress. To avoid the intervention of the effect of end group chirality, crystals obtained from these samples (meso) were further subjected to the present studies. DFT calculations revealed low-lying LUMOs (−3.70, −3.86, −3.94 eV for EHNDI, $EHNDIBr_2$, and $EHNDIBr_4$, respectively) and localized FMOs within the aromatic enclosures (Scheme 1b). The role of Br atoms in the HOMO indicated a hybrid n–π nature for the FMOs in substituted derivatives. The molecular electrostatic potential (ESP) was mapped (Fig. 1a–c) upon sequentially substituting core-hydrogens with Br atoms to understand their role in forming 2-D networks. In $EHNDIBr_2$, large positive (δ^+) potentials at the H atoms (π-core) and largely negative (δ^-) potentials at O atoms and slightly positive and negative potentials at two different faces of Br atoms, respectively, are distinctly visible (Fig. 1b). As a result, $EHNDIBr_2$ π-cores consist of 2-fold C–Br···H and 2-fold C–Br···O attractive interactions between the neighboring lateral pair of molecules preventing considerable longitudinal misalignment (*L*) (Fig. 1e). The lower longitudinal misalignment due to multiple non-covalent interactions and strongly interconnected 2-D brickwork stacks was evident in the crystal packing (*vide infra*). This extended, 2-D network is expected to facilitate bulk electron transport and inhibit lattice vibrations.[30a,b] In contrast, the scenario was entirely different for the other two derivatives (EHNDI and $EHNDIBr_4$). Considerable longitudinal slip was evident due to the mismatch in the lateral interactions. Distinct δ^+ and δ^- charges were present over the H and O atoms, leading to 2-fold C–H···O associative interactions across the lateral neighbors (in EHNDI), whereas a distinct δ^- on the O atom and δ^+ at the front face of the Br atom (Fig. 1c) were evident in $EHNDIBr_4$ resulting in 2-fold C–Br···O intermolecular interactions between the neighboring pair. In both EHNDI and $EHNDIBr_4$, relatively high longitudinal misalignment (Fig. 1d and f) is envisaged compared to $EHNDIBr_2$. More significant longitudinal

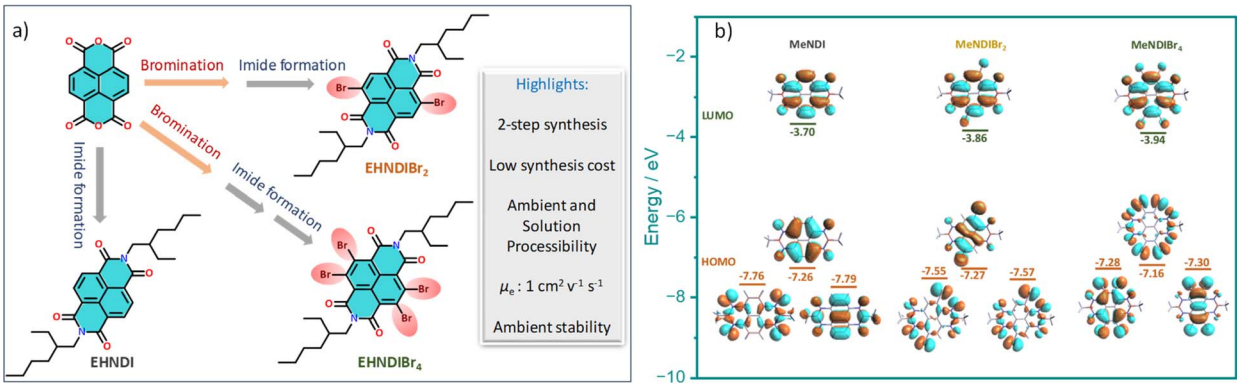

Scheme 1 (a) Structure and the speciality of the NDI derivatives under study and (b) computed frontier molecular orbital (FMO) distributions for three compounds with Me-side chains. Core Br-substituted NDI molecules indicating the contribution of the halogen groups' non-bonding orbitals to the HOMO in the last two cases.

misalignments would reduce the 2-D lateral aggregation, and poor orbital overlap among π-stacked molecules is anticipated in the latter pair, decreasing the 2-D bulk electron transport. Spectroscopic studies were conducted to explore these derivatives' self-assembly features and electronic states, providing insights into their potential for efficient charge transport in semiconductor applications.

Optical and photophysical features

Optical properties of these NDI derivatives would offer valuable insights into their molecular assembly pathways. These properties were studied by UV-VIS absorption and PL spectroscopy using monomeric and aggregated films. Dilute chloroform solutions and thin film samples (Fig. 2a–c) were used. Introducing bromine atoms into the NDI core led to a redshift in the absorption band edge and a reduction in the optical bandgap (E_g). An additional transition, originating from Br-centered non-bonding orbitals, was predicted based on natural transition orbital (NTO) calculations (Fig. 2e). For $EHNDIBr_2$ in $CHCl_3$, we observed well-defined vibronic bands at 408 nm (0–0), 387 nm (0–1), and 364 nm (0–2), and a broader band at 349 nm. The thin film absorption spectra showed an 18 nm redshift in the 0–0 absorption band compared to the monomeric solution state, and the intensity ratio of this band (I_{0-0}/I_{0-1}) increased from 1.13 to 2.6, transitioning from the monomeric solution state to the film state. This shift suggested strong excitonic coupling in densely packed chromophores in film state samples.[31] Corresponding vibronic bands in the film were at 426 nm (0–0), 398 nm (0–1), and 345 nm (0–2). For EHNDI films, the shift was less pronounced, only 9 nm (0–0) compared to the solution state (from 381 nm to 390 nm). $EHNDIBr_4$ showed a 2 nm redshift, and its spectral profile in the film state was similar to the monomeric solution state, indicating minimal excitonic coupling. Photoluminescence (PL) spectra analysis showed that EHNDI exhibited structured emission in chloroform solution, while exhibiting a broad emission band centered near 460 nm, characteristic of NDI excimer emission. In contrast, the substituted derivatives $EHNDIBr_2$ and $EHNDIBr_4$ displayed non-luminescent behavior in solution, likely due to intersystem crossing and non-radiative triplets under ambient conditions, a phenomenon associated with the presence of heavy atoms like bromine, which can induce spin crossover in the excited state.[32a,b] Further, PL spectra of deaerated toluene solutions were also recorded, revealing intense emission bands at 665 nm

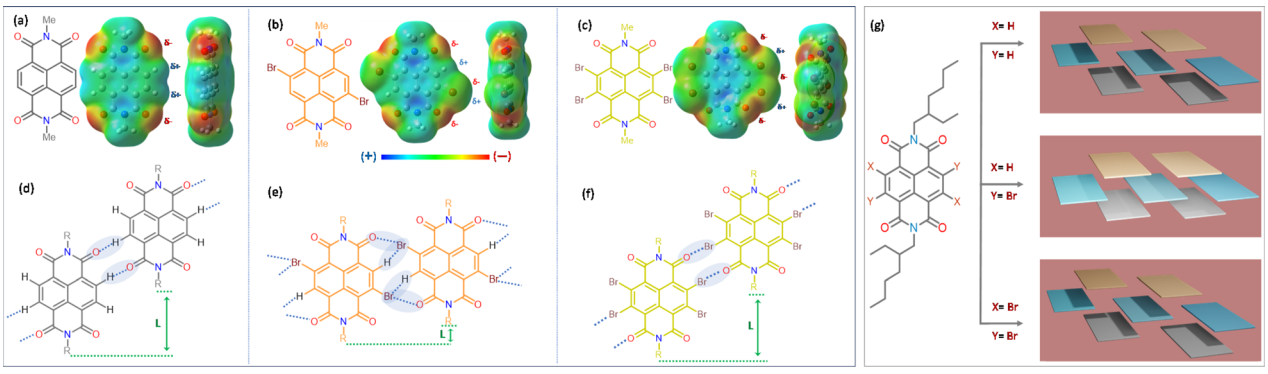

Fig. 1 Chemical structures and ESP maps of (a) MeNDI, (b) $MeNDIBr_2$, and (c) $MeNDIBr_4$ calculated at the B3LYP/6-31+G(d) level of DFT. Schematic lateral interactions, expected from (d) MeNDI, (e) $MeNDIBr_2$, and (f) $MeNDIBr_4$. (g) indicates the different brick-work stacks of molecules in three derivatives under study. Three different colors indicate three layers in each of them.

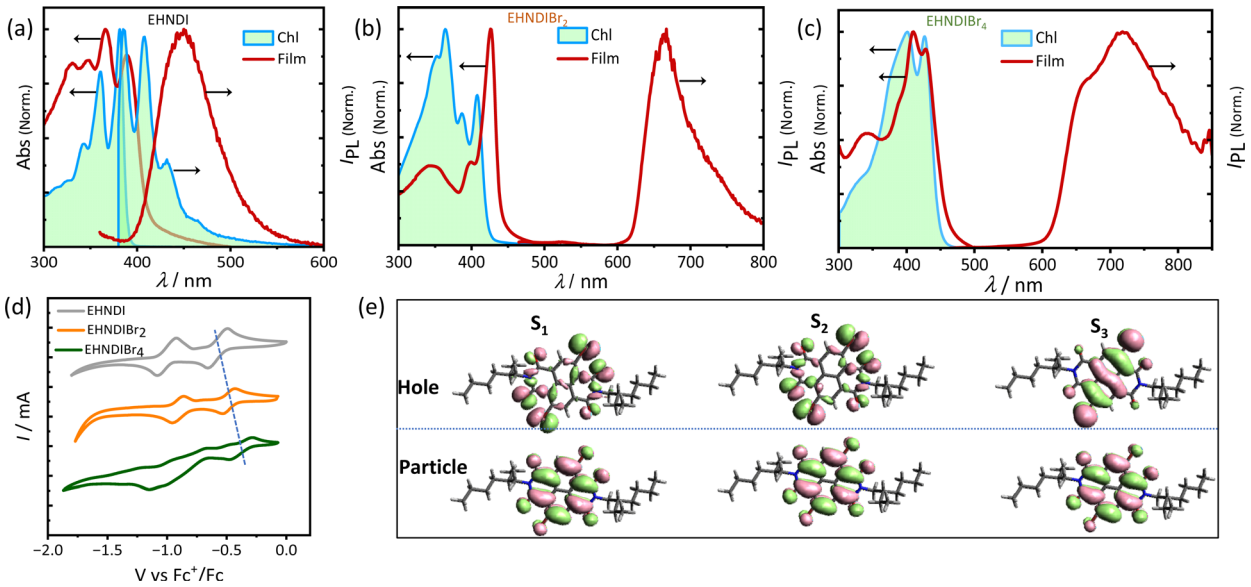

Fig. 2 (a) Solution and film state absorption spectra and emission spectra (a) EHNDI, (b) $EHNDIBr_2$ and (c) $EHNDIBr_4$. (d) Cyclic voltammograms (in reduction cycle) in CH_2Cl_2 solvent (*vs.* Fc/Fc^+) of EHNDI, $EHNDIBr_2$ and $EHNDIBr_4$. (e) The NTO hole and particle distributions in the first, second and third excited states indicating the contribution of Br centric orbitals to the optical transition.

and 715 nm for $EHNDIBr_2$ and $EHNDIBr_4$, respectively (Fig. S8†). This behavior underscores the complexity of the photophysical properties of NDI derivatives and their potential applications in electronic devices, where understanding and manipulating such properties are crucial for optimizing their performance. Overall, the optical studies demonstrate the significant impact of bromine substitution on the electronic structure and excitonic interactions and provide insights into the intricate interplay between the molecular structure, assembly, and photo-physics.

Electrochemical and thermal properties

Electrochemical redox properties of these derivatives were analysed using cyclic voltammetry (CV) in dichloromethane (CH_2Cl_2) at 25 °C, with gold (Au), silver/silver chloride (Ag/AgCl), and platinum (Pt) serving as the working, reference, and counter electrodes, respectively. The CV results (Fig. 2d) revealed two electron reversible reduction peaks, indicating the high electron affinity of these molecules. Consistent with expectations, bromination of the NDI core successively reduced the first onset reduction potential, indicating a deeper LUMO (Lowest Unoccupied Molecular Orbital) level upon introducing electronegative atoms into the core. The LUMO levels were calculated to be −3.82, −3.92, and −4.02 eV for EHNDI, $EHNDIBr_2$, and $EHNDIBr_4$, respectively, using ferrocene (Fc)/ferrocenium (Fc^+) as an internal standard.[33] These compounds' Ionization Potential (IP) values were estimated using Ultraviolet Photoelectron Spectroscopy (UPS). A progressive reduction in IP values was observed with adding bromine atoms, as shown in Fig. S10† and summarized in Table 1. The experimentally obtained parameters, including the HOMO (Highest Occupied Molecular Orbital), and values from CV and optical bandgap measurements, correlated well with the computed values. Further analysis of the materials' physical properties was conducted using Differential Scanning Calorimetry (DSC) and Thermal Gravimetric Analysis (TGA). All three compounds displayed high thermal stability (Fig. S9†), with decomposition onset temperatures exceeding 320 °C (T_d). DSC analysis revealed the melting temperatures (T_m) of the molecules, with $EHNDIBr_2$ exhibiting the highest melting temperature at 253 °C, compared to EHNDI (201 °C) and $EHNDIBr_4$ (approximately 244 °C), despite variations in molecular mass. Intriguingly, the corresponding enthalpy changes (ΔH_m) also showed notable differences. $EHNDIBr_2$ had the highest melting enthalpy change at 53 kJ mol^{-1}, which was 15% greater than that of $EHNDIBr_4$ and 66% higher than that of EHNDI. These superior thermal parameters of $EHNDIBr_2$ solids are attributed to the highest lattice energy among the derivatives, resulting from its unique structural features. The higher melting enthalpy indicates a more rigidly packed structure of $EHNDIBr_2$ in the solid state, potentially contributing to lower effective lattice vibrations. This observation is consistent with the findings from single crystal structure analysis. Consequently, these structural characteristics of $EHNDIBr_2$ contribute to its superior charge carrier transport properties, demonstrating its potential for efficient and stable performance in electronic devices.

OFET device and charge transport characteristics

Organic field-effect transistors (OFETs) with bottom-gate top-contact (BG-TC) geometry were fabricated using solution-processed active layers. These layers were deposited by spin-coating 4–5 mg mL^{-1} chloroform (CHL) solutions of the molecules on *n*-octadecyltrichlorosilane (*n*-OTS) modified Si/SiO_2 substrates.[34] Optimal post-deposition thermal annealing conditions were determined for each derivative: 150 °C for $EHNDIBr_2$, none for EHNDI, and 80 °C for $EHNDIBr_4$. Gold (Au)

Table 1 Summary of the molecular properties in solution and solid-states and the computed HOMO/LUMO levels for the NDI derivatives

	Solution			Solid-state				Computed	
	LUMO[a] [eV]	HOMO[a,b] [eV]	E_g[b] [eV]	IP[c] [eV]	T_m[d] [°C]	ΔH_m[d] [kJ mol^{-1}]	T_d[e] [°C]	HOMO [eV]	LUMO [eV]
EHNDI	−3.8	−7.0	3.2	7.4	201	32	323	−7.3	−3.7
$EHNDIBr_2$	−3.9	−6.9	2.9	7.3	253	53	366	−7.3	−3.9
$EHNDIBr_4$	−4.0	−6.8	2.8	7.2	244	46	322	−7.2	−3.9

[a] Extracted from CV. [b] From UV absorption. [c] Estimated from UPS experiments. [d] Estimated from DSC experiments. [e] Measured from TGA experiments. ΔH_m: enthalpy changed during melting. E_g: optical bandgap.

source–drain (S–D) electrodes were then thermally evaporated onto the substrates. The $EHNDIBr_2$ active layers exhibited impressive dopant-free electron mobility (μ_e) in the saturation regime, reaching up to 1.0 cm^2 V^{-1} s^{-1}, with an average mobility of 0.71 cm^2 V^{-1} s^{-1} across 12 devices. This performance included a high on–off current ratio ($I_{on}/I_{off} > 10^8$) and low hysteresis. In contrast, EHNDI and $EHNDIBr_4$ showed significantly reduced carrier mobility, orders of magnitude lower than that of $EHNDIBr_2$, with the best devices achieving μ_e values of 1.8×10^{-2} cm^2 V^{-1} s^{-1} and 4.5×10^{-3} cm^2 V^{-1} s^{-1}, respectively. Fig. 3 summarizes representative transfer and output characteristics of $EHNDIBr_2$, and the summary of device performance is provided in Table 2. This considerable variation in carrier mobilities among the derivatives is primarily attributed to differences in π-overlap between neighboring molecules in their solid-state structures, as determined by film X-ray diffraction (GIXD and WAXD) measurements. $EHNDIBr_2$'s higher order of molecular assembly and higher degree of aggregation in the film state, compared to EHNDI and $EHNDIBr_4$, result in superior charge transport. All devices exhibited high threshold voltage (V_{th}), regardless of the processing conditions, indicating high contact resistance due to an electron injection barrier at the semiconductor-S-D electrode interface. This suggests poor energy level alignment, potentially caused by mismatched work functions, interfacial and bulk traps, and interface morphology.[35a,b] Efforts are ongoing to minimize contact resistance and improve the threshold voltage.

A reliability factor (r) was introduced to ensure accuracy in carrier mobility extraction, accounting for high V_{th} in devices.[36] The r factors were found to be 30 ± 2% for all devices. $EHNDIBr_2$'s high carrier mobility is credited to its low π-stacking distance, significant π-overlap, low in-plane molecular slip, and well-organized packing in the film state, as observed in single crystal structural analysis and GIXRD measurements. It is known that in the brickwork stack of planar aromatic diimides, the long-axis displacement between the neighboring pair in a π-stack affects the charge transfer integral more intensely than the short-axis displacement.[30a] The same hypothesis can be extended to the above example of $EHNDIBr_2$. Ambient stability was also assessed for these OFET devices, considering that a deep LUMO (<−4.0 eV) is crucial for operational stability.[37] Electrical characterization over 100 hours under ambient conditions (75% humidity) showed that the average charge carrier mobility after 85 hours remained around 16%, 66%, and

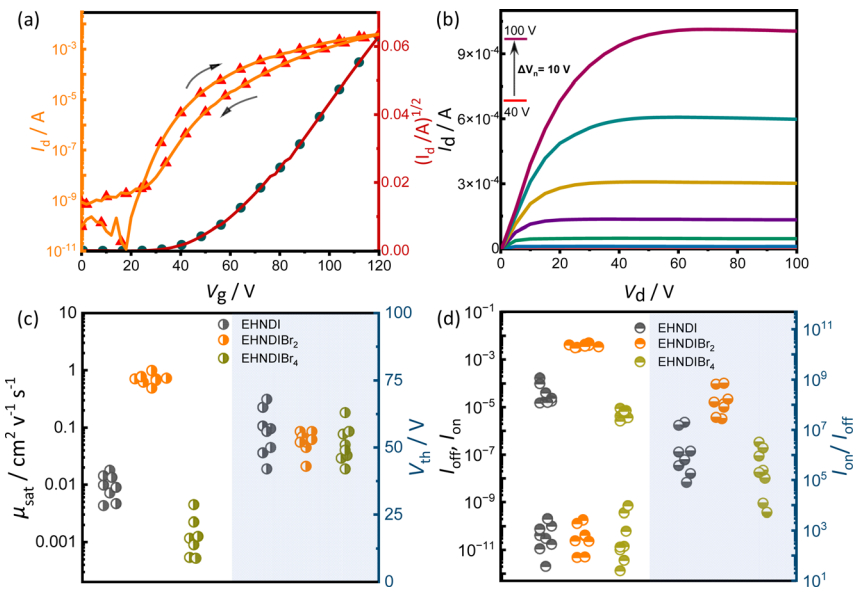

Fig. 3 OFET (a) transfer curve and (b) output curves for the $EHNDIBr_2$ thin film. (c) μ_{sat} (left) and V_{th} (right) variations of EHNDI, $EHNDIBr_2$, and $EHNDIBr_4$ devices. (d) Ion (top left), I_{off} (bottom left), and I_{on}/I_{off} (right) variations of EHNDI, $EHNDIBr_2$, and $EHNDIBr_4$ devices.

Table 2 Summary of the performances of OFET devices, prepared under optimized conditions and their ambient storage stability (75% atmospheric humidity)[a]

	Annealing T/°C	μ_e^{avg} (cm^2 V^{-1} s^{-1})	μ_e^{max} (cm^2 V^{-1} s^{-1})	V_{th} (V)	I_{ON}/I_{OFF}	μ_e^{avg} retention (%)
EHNDI	NA	0.9×10^{-2}	1.8×10^{-2}	56	$>10^7$	16
$EHNDIBr_2$	150	0.71	1.0	52	$>10^8$	66
$EHNDIBr_4$	80	1.6×10^{-3}	4.5×10^{-3}	49	$>10^6$	67

[a] Mobility retention (in %) after 85 h.

67% for EHNDI, $EHNDIBr_2$, and $EHNDIBr_4$, respectively (Fig. 4a). $EHNDIBr_2$ and $EHNDIBr_4$'s better ambient stability is attributed to the hydrophobic effect of Br atoms in the NDI core and their low-lying LUMO levels, which likely hinder moisture diffusion and interfacial charge trapping.

The EHNDI-based devices degraded under ambient exposure, indicating faster air/moisture diffusion and reactivity as EHNDI has higher LUMO values and no hydrophobic groups in the core. The average threshold voltage shifts (ΔV_{th}) were 43 V, 15 V and 13 V for EHNDI, $EHNDIBr_2$ and $EHNDIBr_4$, respectively (Fig. 4b). This possibly indicates the incorporation of charge-trapping states at the dielectric/active layer interface from the atmosphere and the damage of the metal-OSC interfaces by the air. The damage is highest in the case of EHNDI and lowest for $EHNDIBr_4$.

Single crystal structure analysis

The study of solid-state molecular interactions and packing in EHNDI, $EHNDIBr_2$ and $EHNDIBr_4$ was conducted using single-crystal X-ray diffraction experiments (CCDC numbers: 2346855, 2323962, 2323963).† All three compounds crystallized in the triclinic space group $P\bar{1}$. The molecular structure of EHNDI demonstrates planar conformations of the NDI core. Intermolecular interactions primarily involve C–H···O attractive forces, with a distance measuring 2.45 Å (Fig. 5a and S14†). The interplanar π–π stacking distance is around 3.3 Å. In the molecular structure of $EHNDIBr_2$, the NDI core also exhibits planar conformations. The intermolecular interactions are characterized mainly by two types of attractive forces: C–H···Br (with a distance of 2.94 Å) and C–Br···O (3.14 Å) interactions (Fig. 5b and S14†). These distances are shorter than the summation of their van der Waals radii (H···Br = 3.05 Å and Br···O = 3.37 Å),[50] indicating efficient intermolecular interactions, resulting in the low longitudinal misalignment (L) of two lateral neighbors. Additionally, a noticeable intermolecular steric hindrance and structural locking among the adjacent molecules were evident, which also imparted additional stability to the molecular stack. Precisely speaking, the hindrance was among the branched ethyl unit of the side chains between the neighboring molecules and an ethyl–hexyl unit of a molecule, and the core substituted Br atom of the same (Fig. 5d). These steric and intermolecular interactions helped to lock the dimers, minimizing longitudinal slip along the long molecular axis. The low longitudinal misalignment (L) between lateral neighbors enhances π-stacking, while steric hindrance and structural locking among adjacent molecules provide additional stability to the molecular stack. This unique arrangement results in effective π-overlap between adjacent stacks, leading to asymmetric π-stacks with low displacement values of 0.79 and 0.82 Å. The 2-D brickwork packing in $EHNDIBr_2$, characterized by face-to-face stacking and molecular

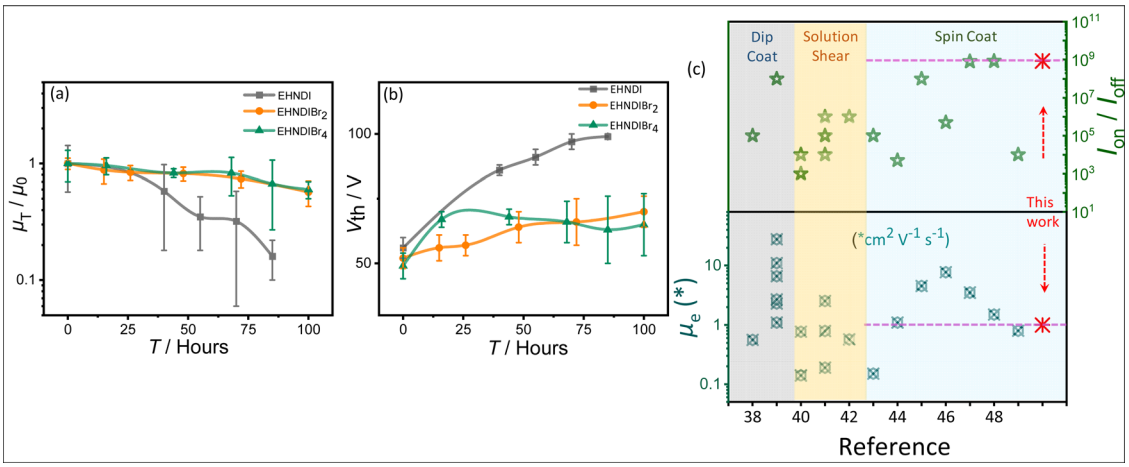

Fig. 4 Ambient stability measurement: (a) average saturation mobility change and (b) the threshold voltage changes (ΔV_{th}) with time of the OFET devices with exposure to the ambient atmosphere. (c) Summarized literature reports on the best device performances.[38–49] PVD processed and single crystal devices excluded.

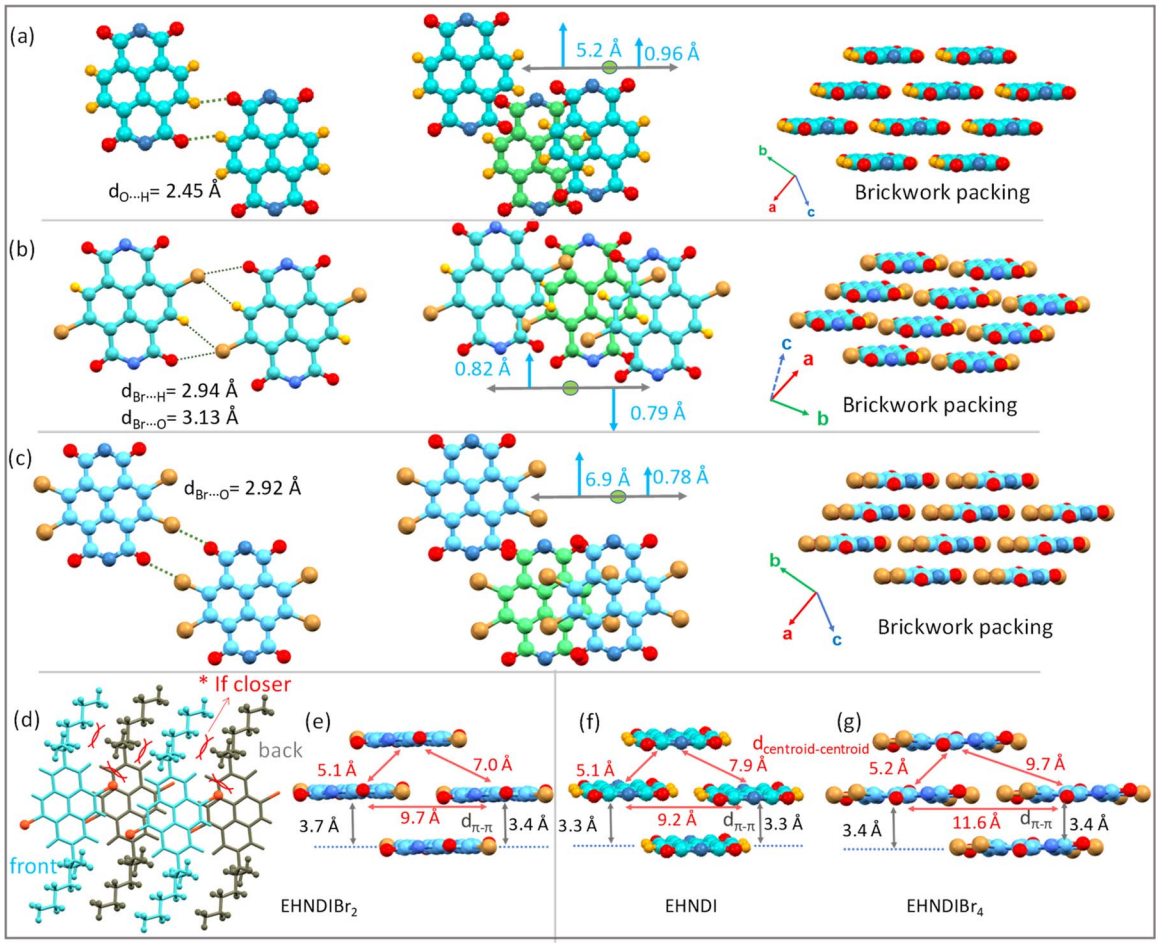

Fig. 5 Single crystal molecular packing and 2-D brickwork packing motifs for EHNDI, $EHNDIBr_2$ and $EHNDIBr_4$: lateral intermolecular interactions, short contacts and packing motifs for (a) EHNDI, (b) $EHNDIBr_2$ and for (c) $EHNDIBr_4$. (d) Representation of the steric locking in $EHNDIBr_2$. Nearest neighbor intermolecular distances in the adjacent stacks for (e) $EHNDIBr_2$, (f) EHNDI and (g) $EHNDIBr_4$.

overlaps, contributes to its high charge carrier mobility. In contrast, $EHNDIBr_4$ exhibits major lateral interactions such as C–O···Br (around 2.92 Å) and C–H···Br (2.91 Å) (alkyl chain H) (Fig. 5c and S14†). However, the absence of (i) core-bromines in EHNDI and (ii) core-hydrogens in $EHNDIBr_4$ results in different interaction possibilities compared to $EHNDIBr_2$, leading to a relatively large longitudinal displacement in the former pair. Despite a short inter-planar distance (3.3–3.4 Å) (Fig. 5f and g), EHNDI and $EHNDIBr_4$ show a mix of good and minimal π-overlap in their asymmetric π-stacks, which affects their charge transport properties. The presence of one stack with low L (approximately 0.96 Å and 0.78 Å for EHNDI and $EHNDIBr_4$ respectively) indicates good π-overlap, while another stack with high L (approximately 5.2 Å and 6.9 Å for EHNDI and $EHNDIBr_4$ respectively) shows minimal overlap, resulting in weaker 2-D charge transport features for both EHNDI and $EHNDIBr_4$. The increased displacement observed in $EHNDIBr_4$ compared to EHNDI suggests even poorer charge transport in $EHNDIBr_4$, a conclusion supported by the device results. These findings demonstrate how the molecular structure and intermolecular interactions within the solid-state significantly influence the electronic properties of these materials, particularly in relation to their charge transport capabilities. The distinct molecular arrangements and packing in EHNDI, $EHNDIBr_2$ and $EHNDIBr_4$ lead to notably different electronic performances, with $EHNDIBr_2$ showing superior charge carrier mobility due to its more effective π-stacking and molecular interactions.

Film state WXRD and GIXRD

Out-of-plane wide-angle XRD measurements (WXRD) were conducted on OTS-modified Si/SiO_2 substrates (Fig. S15h†). Considering the molecular dimensions, plausible molecular stacking on substrates was simulated following known reports of NDI-derived materials. At first glance, $EHNDIBr_2$ films exhibited more crystalline domains than the other two, considering the higher order of diffraction from its sample surface. Considering the d-values of the first-order signal and the molecular dimension (end-to-end distance of ~21.5 Å as obtained from their single crystal structures), along with the absence of reflection due to π–π ordering (around $2\theta = 25°$–$30°$), we confirmed that vertical molecular alignment on the substrate surface (ordering along 001) is prevailing. Higher-order reflections indicating extended periodicity along the

vertical direction confirmed well-organized lamellar supramolecular structures of $EHNDIBr_2$ on the substrate surface. The position of the first-order signal for the latter pair was at $2\theta = 5.8–6.1°$, whereas it was 4.28° for $EHNDIBr_2$. This difference in the first-order reflection position for the former pair is attributed primarily to the inclined molecular long axis on the surface, as indicated in Fig. S15.† Comparing the molecular length and the first-order reflections, a relative inclination of the molecular long axis is predicted to be ~73° for $EHNDIBr_2$ and ~43°–45° for the other two derivatives. Further, on comparing the simulated powder XRD patterns from the SCXRD data and the experimentally obtained film state WAXRD of $EHNDIBr_2$, we confirmed that the planes (00*N*) were positioned parallel to the substrate with the unit cell axes *a* and *b* on the parallel plane. Subsequently, $EHNDIBr_2$ molecules are positioned on the substrate surface with the π–π stacking direction parallel to the substrate surface, which helps to achieve excellent 2D charge transport.

To understand the in-plane periodicity in the bulk films deposited on the substrates, and alterations of the diverse packing patterns, including molecular orientations, GIXRD measurements were conducted on oxide substrates. $EHNDIBr_2$ films exhibited in-plane and out-of-plane (q_z and q_{xy}) ordering indicative of strong signals, as shown in (Fig. 6b and S15†). In contrast, weak in-plane diffractions were observed in the case of the EHNDI-film, indicating weak long-range in-plane ordering and no out-of-plane signals were observed, indicating extremely weak lamellar ordering along the vertical direction. For $EHNDIBr_4$ films, neither in-pane nor out-of-plane signals were evident, which confirms a highly amorphous character (Fig. 6c and S15†) as indicated in the WXRD experiment (*vide supra*). Additionally, the (*00l*) ordered patterns along q_z were visibly spotted for $EHNDIBr_2$ films (Fig. 6d), which appeared as higher ordered (001) to (004) peaks, inferring a controlled edge-on molecular orientation (Fig. 6f). The conjugated backbones are aligned perpendicular to the substrate, having strong intermolecular π-stacking interactions, which is the most favorable condition for lateral charge transport in devices such as OFETs. The q_z *d*-spacing (from (001) peak) of 20.3 Å again confirmed that the molecular long axis is positioned at nearly 71° tilt angle (as the molecular length of 21.5 Å). The q_{xy} *d*-spacing value calculated from the (20*l*) peak of the in-plane profile (Fig. 6e) is 3.6 Å, signifying π–π stacking distances, which endorse the value obtained from a single crystal structure. The 2-D diffraction profile of EHNDI indicated less ordering in their film states with a minimum *d*-spacing of 4.1 Å in q_{xy} (Fig. S15†). On the other hand, $EHNDIBr_4$ displayed only (001) diffraction spots lacking higher-order signals, indicating a lack of periodic ordering in both the lateral (*xy*) and *z* directions. To summarize, $EHNDIBr_2$ is expected to have the most favorable molecular orientation on surfaces to facilitate the charge carrier transport, while $EHNDIBr_4$ has the least.

AFM and SEM analysis

To understand the effect of film morphologies on charge transport, atomic force microscopy (AFM) and scanning electron microscopy (SEM) experiments were carried out on the films, keeping the device deposition condition fixed. Fig. 7 shows AFM and SEM images for all three molecules. Fig. 7a shows the large micron-size grains in the film state of EHNDI with a few visible grain boundaries, whereas many small grains (~80–100 nm) containing large numbers of boundaries were observed in the case of $EHNDIBr_4$ (Fig. 7c). Significant grain boundaries create high resistance for charge transport through the bulk, which is observed in the lowest μ_e value of $EHNDIBr_4$.[42,51] Both the compounds contain relatively higher roughness (root-mean-square (RMS) roughness, EHNDI: 4.8 nm

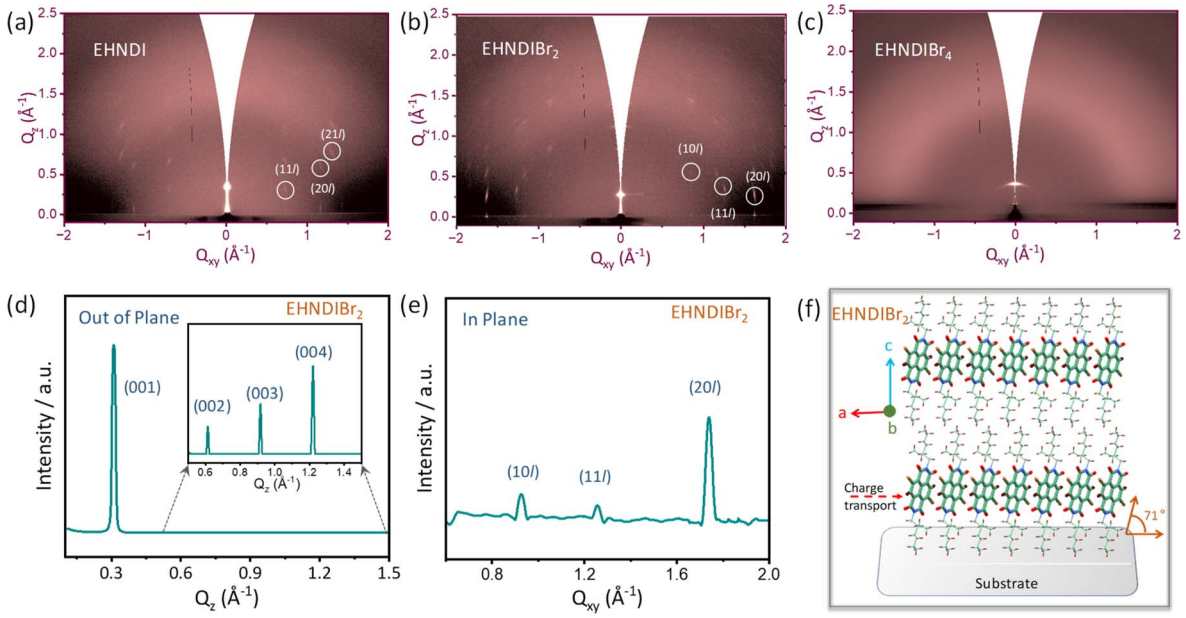

Fig. 6 (a–c) 2-D GIXRD diffraction profile of the optimized samples, (d) and (e) 1-D line cut profile of the $EHNDIBr_2$ films: (e) in-plane and (d) out-of-plane indicating periodic reflections of 001 planes. (f) Plausible molecular ordering on the surface.

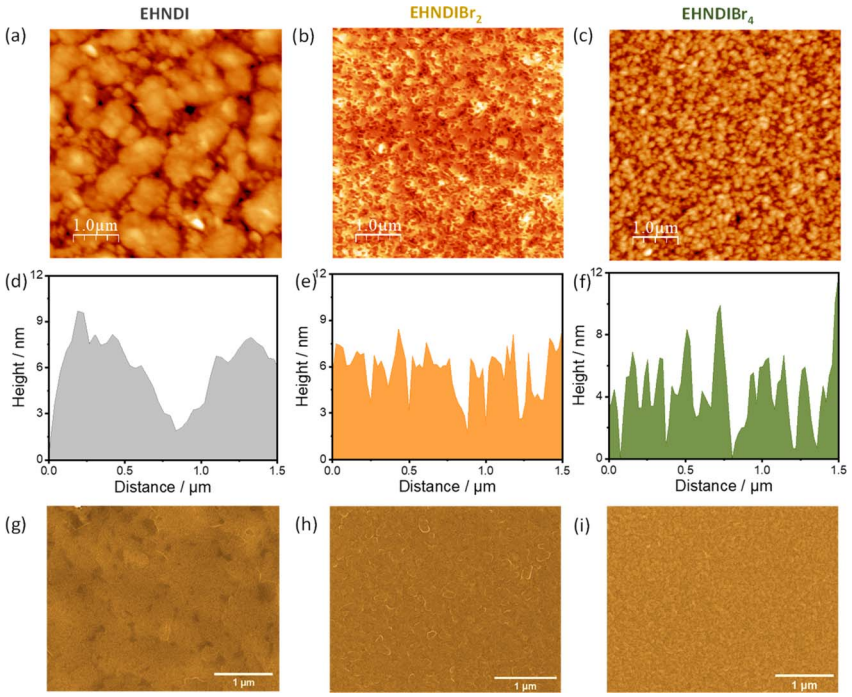

Fig. 7 AFM topography images, AFM height profiles and SEM images (a), (d), and (g) for EHNDI, (b), (e), and (h) for $EHNDIBr_2$ and (c), (f), and (i) for $EHNDIBr_4$ respectively.

and $EHNDIBr_4$: 3.18 nm) than $EHNDIBr_2$ (RMS: 2.66 nm). $EHNDIBr_2$, consisting of highly crystalline domains in the film state (Fig. 7b), shows a relatively smooth surface with very few grain boundaries, which is favourable for excellent charge transport.

Conclusion

The structural requirements of efficient n-type organic semiconductors and their device characteristics are summarized here. A simple and known skeletal unit (NDI) was considered for the case study, and the core unit was derivatized by Br atom substitution to yield three derivatives for studies. The most efficient candidate ($EHNDIBr_2$) in terms of processibility, superior carrier mobility and ambient stability was subjected to critical analysis. Brickwork supramolecular stacks were confirmed by single crystal XRD studies. Interestingly, rigid in-plane molecular ordering originated from steric locking mode, and multiple favourable non-covalent interactions were holding the molecular hoping centres, minimizing the longitudinal dimeric slip, and possibly lowering the thermal oscillations in the bulk lattice. The structural and stability of the samples were confirmed by a detailed thermal analysis. Our multi-faceted approach on picking up the right molecular unit is expected to trigger a new design strategy. We expect that our report on n-type molecular semiconductors substantially advances organic electronics.

Data availability

The data (experimental procedures, characterization data and DFT calculations) that support this article is available within the article and its ESI.†

Author contributions

IG, SC, and JJP conducted the synthesis and characterization of all compounds. IG has performed electrical characterizations, single crystal packing analysis, microscopy, 2D GIXRD, optical and electrochemical experiments and analysis, as well as DFT-ESP calculations. MM performed the NTO calculation. ABD provided guidance for 2D GIXRD experiments and analysis. RV conceptualized and supervised the project.

Conflicts of interest

The authors declare no competing financial interests.

Acknowledgements

IG and JJ thank UGC, and SC and MM thank CSIR-India for their fellowships. This work was supported by IGSTC 2+2 LABELONIK and CRG/2021/006054. We acknowledge DESY (Hamburg, Germany), a member of the Helmholtz Association HGF, for the provision of experimental facilities. Parts of this research were carried out at the P08 beamline, PETRA III, DESY, Germany. Beamtime was allocated for proposal(s) (project no. I-20221013, I-20211469). We acknowledge financial support by the Department of Science & Technology, Government of India (DST),

provided within the framework of the India@Desy collaboration. We also acknowledge Dr Surojit Bhunia and Mr Kaustav Das for helping in solving crystal structures. The authors thank Dr Rahul Banerjee for the fruitful discussions.

References

1 J. Chen, W. Zhang, L. Wang and G. Yu, *Adv. Mater.*, 2023, **35**, 2210772.
2 H. Katz, A. Lovinger, J. Johnson, C. Kloc, T. Siegrist, W. Li, Y. Lin and A. Dodabalapur, *Nature*, 2000, **404**, 478–481.
3 D. Shukla, S. F. Nelson, D. C. Freeman, M. Rajeswaran, W. G. Ahearn, D. M. Meyer and J. T. Carey, *Chem. Mater.*, 2008, **20**, 7486–7491.
4 D. Bialas, E. Kirchner, M. I. S. Röhr and F. Würthner, *J. Am. Chem. Soc.*, 2021, **143**, 4500–4518.
5 M. M. Ling, P. Erk, M. Gomez, M. Koenemann, J. Locklin and Z. Bao, *Adv. Mater.*, 2007, **19**, 1123–1127.
6 X. Cui, C. Xiao, T. Winands, T. Koch, Y. Li, L. Zhang, N. L. Doltsinis and Z. Wang, *J. Am. Chem. Soc.*, 2018, **140**, 12175–12180.
7 A. Velusamy, C. H. Yu, S. N. Afraj, C. C. Lin, W. T. Lo, C. J. Yeh, Y. W. Wu, H. C. Hsieh, J. Chen, G. H. Lee, S. H. Tung, C. L. Liu, M. C. Chen and A. Facchetti, *Adv. Sci.*, 2021, **8**, 2002930.
8 S. Fratini, M. Nikolka, A. Salleo, G. Schweicher and H. Sirringhaus, *Nat. Mater.*, 2020, **19**, 491–502.
9 J. E. Anthony, J. S. Brooks, D. L. Eaton and S. R. Parkin, *J. Am. Chem. Soc.*, 2001, **123**, 9482–9483.
10 M. Mas-Torrent and C. Rovira, *Chem. Rev.*, 2011, **111**, 4833–4856.
11 K. J. Kalita, I. Giri and R. K. Vijayaraghavan, *RSC Adv.*, 2021, **11**, 33703–33713.
12 R. Kroon, D. A. Mengistie, D. Kiefer, J. Hynynen, J. D. Ryan, L. Yu and C. Müller, *Chem. Soc. Rev.*, 2016, **45**, 6147–6164.
13 (*a*) C. Luo, A. K. K. Kyaw, L. A. Perez, S. Patel, M. Wang, B. Grimm, G. C. Bazan, E. J. Kramer and A. J. Heeger, *Nano Lett.*, 2014, **14**, 2764–2771; (*b*) K. Liu, B. Ouyang, X. Guo, Y. Guo and Y. Liu, *npj Flexible Electron.*, 2022, **6**, 1; (*c*) T. Okamoto, S. Kumagai, E. Fukuzaki, H. Ishii, G. Watanabe, N. Niitsu, T. Annaka, M. Yamagishi, Y. Tani, H. Sugiura, T. Watanabe, S. Watanabe and J. Takeya, *Sci. Adv.*, 2020, **6**, eaaz0632.
14 P. A. Banks, G. D'Avino, G. Schweicher, J. Armstrong, C. Ruzié, J. W. Chung, J. Park, C. Sawabe, T. Okamoto, J. Takeya, H. Sirringhaus and M. T. Ruggiero, *Adv. Funct. Mater.*, 2023, **33**, 2303701.
15 T. Hodsden, K. J. Thorley, J. Panidi, A. Basu, A. V. Marsh, H. Dai, A. J. P. White, C. Wang, W. Mitchell, F. Glöcklhofer, T. D. Anthopoulos and M. Heeney, *Adv. Funct. Mater.*, 2020, **30**, 2000325.
16 M. A. Stoeckel, Y. Olivier, M. Gobbi, D. Dudenko, V. Lemaur, M. Zbiri, A. A. Y. Guilbert, G. D'Avino, F. Liscio, A. Migliori, L. Ortolani, N. Demitri, X. Jin, Y. G. Jeong, A. Liscio, M. V. Nardi, L. Pasquali, L. Razzari, D. Beljonne, P. Samorì and E. Orgiu, *Adv. Mater.*, 2021, **33**, 2007870.
17 C. P. Yu, S. Kumagai, T. Kushida, M. Mitani, C. Mitsui, H. Ishii, J. Takeya and T. Okamoto, *J. Am. Chem. Soc.*, 2022, **144**, 11159–11167.
18 J. H. Dou, Z. A. Yu, J. Zhang, Y. Q. Zheng, Z. F. Yao, Z. Tu, X. Wang, S. Huang, C. Liu, J. Sun, Y. Yi, X. Cao, Y. Gao, J. Y. Wang and J. Pei, *J. Am. Chem. Soc.*, 2019, **141**, 6561–6568.
19 J. E. Anthony, *Chem. Rev.*, 2006, **106**, 5028–5048.
20 T. Yamamoto and K. Takimiya, *J. Am. Chem. Soc.*, 2007, **129**, 2224–2225.
21 H. Sirringhaus, *Adv. Mater.*, 2014, **26**, 1319–1335.
22 H. Iino, T. Usui and J. I. Hanna, *Nat. Commun.*, 2015, **6**, 6828.
23 B. A. Jones, M. J. Ahrens, M. H. Yoon, A. Facchetti, T. J. Marks and M. R. Wasielewski, *Angew. Chem., Int. Ed.*, 2004, **43**, 6363–6366.
24 T. He, M. Stolte and F. Würthner, *Adv. Mater.*, 2013, **25**, 6951–6955.
25 J. M. Mativetsky, E. Orgiu, I. Lieberwirth, W. Pisula and P. Samorì, *Adv. Mater.*, 2014, **26**, 430–435.
26 K. Shi, W. Zhang, D. Gao, S. Zhang, Z. Lin, Y. Zou, L. Wang and G. Yu, *Adv. Mater.*, 2018, **30**, 1705286.
27 L. T. Ming, H. O. Joon, A. D. Reichardt and Z. Bao, *J. Am. Chem. Soc.*, 2009, **131**, 3733–3740.
28 S. Kumagai, H. Ishii, G. Watanabe, T. Annaka, E. Fukuzaki, Y. Tani, H. Sugiura, T. Watanabe, T. Kurosawa, J. Takeya and T. Okamoto, *Chem. Mater.*, 2020, **32**, 9115–9125.
29 D. Gunturkun, R. Isci, S. Faraji, B. Sütay, L. A. Majewski and T. Ozturk, *J. Mater. Chem. C*, 2023, **11**, 13129–13141.
30 (*a*) M. C. R. Delgado, E. G. Kim, D. A. S. Filho and J. L. Bredas, *J. Am. Chem. Soc.*, 2010, **132**, 3375–3387; (*b*) S. Kumagai, H. Ishii, G. Watanabe, C. P. Yu, S. Watanabe, J. Takeya and T. Okamoto, *Acc. Chem. Res.*, 2022, **55**, 660–672.
31 N. J. Hestand and F. C. Spano, *Chem. Rev.*, 2018, **118**, 7069–7163.
32 (*a*) S. Guo, W. Wu, H. Guo and J. Zhao, *J. Org. Chem.*, 2012, **77**, 3933–3943; (*b*) M. Mondal, I. Giri, R. Patra, M. Das and R. K. Vijayaraghavan, *Chem. Mater.*, 2023, **35**, 6527–6537.
33 B. K. Barman, N. G. Ghosh, I. Giri, C. Kumar, S. S. Zade and R. K. Vijayaraghavan, *Nanoscale*, 2021, **13**, 6759–6763.
34 I. Giri, S. Biswas, S. Chhetri, A. Choudhuri, I. Mondal, S. P Senanayak, P. Krishnan Iyer, D. Chaudhuri and R. K. Vijayaraghavan, *RSC Adv.*, 2024, **14**, 7915–7923.
35 (*a*) M. Waldrip, O. D. Jurchescu, D. J. Gundlach and E. G. Bittle, *Adv. Funct. Mater.*, 2020, **30**, 1904576; (*b*) G. Choi, S. Oh, J. Seo and H. S. Lee, *Adv. Funct. Mater.*, 2020, **30**, 2002979.
36 H. H. Choi, K. Cho, C. D. Frisbie, H. Sirringhaus and V. Podzorov, *Nat. Mater.*, 2018, **17**, 2–7.
37 J. Dhar, U. Salzner and S. Patil, *J. Mater. Chem. C*, 2017, **5**, 7404–7430.
38 H. Reiss, L. Ji, J. Han, S. Koser, O. Tverskoy, J. Freudenberg, F. Hinkel, M. Moos, A. Friedrich, I. Krummenacher, C. Lambert, H. Braunschweig, A. Dreuw, T. B. Marder and U. H. F. Bunz, *Angew. Chem., Int. Ed.*, 2018, **57**, 9543–9547.
39 M. Chu, J. X. Fan, S. Yang, D. Liu, C. F. Ng, H. Dong, A. M. Ren and Q. Miao, *Adv. Mater.*, 2018, **30**, 1803467.
40 S. Vegiraju, A. A. A. Torimtubun, P. S. Lin, H. C. Tsai, W. C. Lien, C. S. Chen, G. Y. He, C. Y. Lin, D. Zheng,

Y. F. Huang, Y. C. Wu, S. L. Yau, G. H. Lee, S. H. Tung, C. L. Wang, C. L. Liu, M. C. Chen and A. Facchetti, *ACS Appl. Mater. Interfaces*, 2020, **12**, 25081–25091.

41 A. Velusamy, C. H. Yu, S. N. Afraj, C. C. Lin, W. Y. Lo, C. J. Yeh, Y. W. Wu, H. C. Hsieh, J. Chen, G. H. Lee, S. H. Tung, C. L. Liu, M. C. Chen and A. Facchetti, *Adv. Sci.*, 2021, **8**, 2002930.

42 W. Y. Lee, J. H. Oh, S. L. Suraru, W. C. Chen, F. Würthner and Z. Bao, *Adv. Funct. Mater.*, 2011, **21**, 4173–4181.

43 P. Kafourou, B. Park, J. Luke, L. Tan, J. Panidi, F. Glöcklhofer, J. Kim, T. D. Anthopoulos, J. S. Kim, K. Lee, S. Kwon and M. Heeney, *Angew. Chem., Int. Ed.*, 2021, **60**, 5970–5977.

44 P. Kafourou, M. I. Nugraha, A. Nikitaras, L. Tan, Y. Firdaus, F. Aniés, F. Eisner, B. Ding, J. Wenzel, M. Holicky, L. Tsetseris, T. D. Anthopoulos and M. Heeney, *ACS Mater. Lett.*, 2022, **4**, 165–174.

45 C. Zhang, D. Yuan, H. Wu, E. Gann, L. Thomsen, C. R. McNeill, C. Di, X. Zhu and D. Zhu, *J. Mater. Chem. C*, 2017, **5**, 1935–1943.

46 Y. Xiong, J. Tao, R. Wang, X. Qiao, X. Yang, D. Wang, H. Wu and H. Li, *Adv. Mater.*, 2016, **28**, 5949–5953.

47 F. Zhang, Y. Hu, T. Schuettfort, C. A. Di, X. Gao, C. R. McNeill, L. Thomsen, S. C. B. Mannsfeld, W. Yuan, H. Sirringhaus and D. Zhu, *J. Am. Chem. Soc.*, 2013, **135**, 2338–2349.

48 G. Liu, C. Xiao, F. Negri, Y. Li and Z. Wang, *Angew. Chem., Int. Ed.*, 2020, **59**, 2008–2012.

49 G. Lin, Y. Qin, J. Zhang, Y. S. Guan, H. Xu, W. Xu and D. Zhu, *J. Mater. Chem. C*, 2016, **4**, 4470–4477.

50 A. Bondi, *J. Phys. Chem.*, 1964, **68**, 441–451.

51 H. H. Choi, A. F. Paterson, M. A. Fusella, J. Panidi, O. Solomeshch, N. Tessler, M. Heeney, K. Cho, T. D. Anthopoulos, B. P. Rand and V. Podzorov, *Adv. Funct. Mater.*, 2020, **30**, 1903617.